

A Residual-Based Procedure for hp-Adaptation on 2D Hybrid Meshes

Haiyang Gao¹ and Z.J. Wang²

Dept. of Aerospace Engineering, Iowa State University, Ames, IA, 50011

H- and p-adaptations are effective ways of achieving high-quality solutions for CFD simulations, with reasonable computing costs. Combined hp-adaptation offers even greater flexibility for complex problems. In the present study, a residual based procedure for hp-adaptation is developed. The adaptation is driven by an efficient multi-p a posteriori error estimator. P-adaptation is applied to smooth regions of the flow field while h-adaptation targets the non-smooth regions, identified by accuracy-preserving TVD marker. Several numerical tests with the correction procedure via reconstruction (CPR) formulation are presented to demonstrate the capability of the technique.

I. Introduction

Adaptive solution methods have been an active topic of CFD research for decades. Through these methods, computing power can be redistributed to where it is needed the most, thus the desired accuracy can be achieved with minimal costs.

For a high-order method, two types of adaptations are usually considered: local mesh subdivision (h-refinement) and local polynomial degree enrichment (p-refinement). It has been shown that p-adaptation is superior in regions where the solution is smooth [13], while h-adaptation is preferred in non-smooth regions such as flow discontinuities, where high-order methods become less effective. Obviously, the combination of both h- and p-adaptation offers greater flexibility than methods that incorporate h- or p-adaptation alone.

Hp-adaptation is made possible by the development of a series of compact high-order methods for unstructured meshes, such as the discontinuous Galerkin (DG) method [3,4,7], the spectral volume (SV) method [14,21] and the spectral difference (SD) method [15]. Unlike the finite volume method that achieve high-order by expanding the stencil, the above methods employ a polynomial to approximate the solution in each cell or element, and the polynomials collectively form a function which is discontinuous across cell boundaries. The compact solution reconstruction of these methods is an ideal feature for p-adaptation. Recently, the correction procedure via reconstruction (CPR) formulation was developed in 1D [11], and extended to simplex and hybrid meshes in [22]. It unites the DG, SV and SD method into a nodal differential formulation. The CPR formulation combines the compactness and high accuracy with the simplicity and efficiency of the finite difference method, and can be easily implemented for arbitrary unstructured meshes. The current hp-adaptation is based on the CPR formulation, but similar methods can be easily applied to other compact high-order methods.

For an hp-adaptation scheme, two indicators need to be computed: a local error indicator to serve as the adaptation criteria, and a local smoothness indicator, used to decide whether h- or p-adaptation should be applied to a certain region.

The error indicator is the foundation of any adaptation method, and finding a reliable error indicator is no trivial task. It seems there are at least three types of adaptation criteria: gradient or feature based error estimate [5,9], residual-based error estimate [1,2,6,17,22], and adjoint-based error estimate [8,10,16,18-20]. The first criteria are the most widely used: it is normally quite easy to implement, since the error indicator is computed directly from solution variables. But the approach is also the most ad-hoc, for it often involves case-dependent parameters. When properly used, it can improve solution quality efficiently [9]. The residual-based error estimate has a variety of forms. It can be used with a multi-grid approach [2], or with an approximate error transport equation [22]. There are also residual estimates based on the solution discontinuity across cell boundaries [17]. For "real world" 3D problems, the multi-grid approach requires the generation of fine grids, which may be difficult to generate. This has probably hindered its wider application. The most successful approach is arguably the adjoint-based approach, which relates a specific

¹Graduate Research Assistant, Dept. of Aerospace Engineering, 2271 Howe Hall, AIAA Member.

²Professor, Dept. of Aerospace Engineering, 2271 Howe Hall, Associate Fellow of AIAA.

functional output, such as the lift or drag coefficient in aerodynamics, directly to the local residual by solving an additional adjoint problem. It has been shown that this approach is very effective in driving an hp-adaptation procedure in obtaining a very accurate prediction of the functional output [18]. The drawback of this approach is that an adjoint problem must be solved, and a functional output is required to drive the adaptation.

In the present study, a residual-based approach using a multi-p error estimation is adopted as the error indicator. This error indicator involves no ad-hoc parameters. It is also much more efficient to compute compared to the adjoint-based approach, since it mostly involves residual evaluation.

For the search of the smoothness indicator, we turn to the solution limiting schemes for high-order methods. The ‘‘troubled cell’’ markers are often used to mark the non-smooth cells before the solution is limited. The accuracy-preserving TVD (AP-TVD) marker [23] is employed in the present study as the non-smoothness indicator, since it does not have case-dependent parameters and can effectively mark the non-smooth regions without marking the smooth extremas. For non-smooth regions, a hierarchical moment limiter [23] is applied to suppress the spurious oscillations.

The rest of the paper is organized as follows: the numerical formulation is presented in Section 2, including a brief review of the CPR formulation, the multi-p error estimation, and the AP-TVD marker. Section 3 is about mesh adaptation strategies, including the treatment of non-conformal interfaces in hp-adaptation and the procedures for hp-adaptation. Several numerical test cases of the inviscid flow are presented in Section 4. Section 5 is devoted to concluding remarks.

II. Numerical Formulation

1. Review of the CPR formulation

Consider the hyperbolic conservation law,

$$\frac{\partial Q}{\partial t} + \vec{\nabla} \cdot \vec{F}(Q) = 0, \quad (2.1)$$

where $\vec{F} = (F, G)$ is the flux vector. The computational domain is discretized into N non-overlapping elements $\{V_i\}$. Let W be an arbitrary weighting function. The weighted residual of Eq. (2.1) on element V_i can be written as

$$\int_{V_i} \left(\frac{\partial Q}{\partial t} + \vec{\nabla} \cdot \vec{F}(Q) \right) W dV = \int_{V_i} \frac{\partial Q}{\partial t} W dV + \int_{\partial V_i} W \vec{F}(Q) \cdot \vec{n} dS - \int_{V_i} \vec{\nabla} W \cdot \vec{F}(Q) dV = 0. \quad (2.2)$$

Let Q_i be an approximate solution to Q at element i . We assume that in each element, the solution belongs to the space of polynomials of degree k or less, i.e., $Q_i \in P^k$, with no continuity requirement across element interfaces. The numerical solution Q_i should satisfy Eq. (2.2), i.e.,

$$\int_{V_i} \frac{\partial Q_i}{\partial t} W dV + \int_{\partial V_i} W \vec{F}(Q_i) \cdot \vec{n} dS - \int_{V_i} \vec{\nabla} W \cdot \vec{F}(Q_i) dV = 0. \quad (2.3)$$

A common Riemann flux across cell interfaces is used to replace the normal flux to provide element coupling, i.e.,

$$\vec{F}(Q_i) \cdot \vec{n} \approx F_{\text{com}}^n(Q_i, Q_{i+}, \vec{n}). \quad (2.4)$$

where Q_{i+} is the solution on V_{i+} , which is outside V_i . Instead of (2.3), the solution is required to satisfy

$$\int_{V_i} \frac{\partial Q_i}{\partial t} W dV + \int_{\partial V_i} W F_{\text{com}}^n dS - \int_{V_i} \vec{\nabla} W \cdot \vec{F}(Q_i) dV = 0. \quad (2.5)$$

Applying integration by parts to the last term on the LHS of (2.4), we obtain

$$\int_{V_i} \frac{\partial Q_i}{\partial t} W dV + \int_{V_i} W \vec{\nabla} \cdot \vec{F}(Q_i) dV + \int_{\partial V_i} W [F_{\text{com}}^n - F^n(Q_i)] dS = 0. \quad (2.6)$$

The last term on the left side of (2.5) can be viewed as a penalty term, i.e., penalizing the normal flux differences. Introduce a “correction field”, $\delta_i \in P^k$, which is determined from a “lifting operator”,

$$\int_{V_i} W \delta_i dV = \int_{\partial V_i} W [F^n] dS, \quad (2.7)$$

where $[F^n] = F_{\text{com}}^n(Q_i, Q^+, \vec{n}) - F^n(Q_i)$ is the normal flux difference. Substituting (2.7) into (2.6), we obtain,

$$\int_{V_i} \left[\frac{\partial Q_i}{\partial t} + \vec{\nabla} \cdot \vec{F}(Q_i) + \delta_i \right] W dV = 0. \quad (2.8)$$

For non-linear fluxes, the flux divergent $\vec{\nabla} \cdot \vec{F}(Q_i)$ is usually not in the space P^k , in which case $\vec{\nabla} \cdot \vec{F}(Q_i)$ is projected to P^k by,

$$\int_{V_i} \Pi(\vec{\nabla} \cdot \vec{F}(Q_i)) W dV = \int_{V_i} \vec{\nabla} \cdot \vec{F}(Q_i) W dV \quad (2.9)$$

Because W is arbitrary, (2.8) is equivalent to

$$\frac{\partial Q_i}{\partial t} + \Pi(\vec{\nabla} \cdot \vec{F}(Q_i)) + \delta_i = 0. \quad (2.10)$$

With the definition of a correction field δ_i , we have successfully reduced the weighted residual formulation to an equivalent simple differential form, which does not involve any explicit surface or volume integrals. The lifting operator obviously depends on the choice of weighting function. If $W \in P^k$, (2.10) is equivalent to the DG formulation. The performance of this formulation of course hinges on how efficiently the correction field δ_i can be computed. If $[F^n]$ is assumed to be degree p polynomials along the cell faces, and that the triangle has straight faces, the correction field δ_i can be computed explicitly in the following form

$$\delta_{i,j} = \frac{1}{|V_i|} \sum_{f \in \partial V_i} \sum_l \alpha_{j,f,l} [F^n]_{f,l} S_f, \quad (2.11)$$

where $\alpha_{j,f,l}$ are constant lifting coefficients independent of the solution, but dependent on the weighting function W . Substituting (2.11) into (2.10) we obtain the following formulation

$$\frac{\partial Q_{i,j}}{\partial t} + \Pi(\vec{\nabla} \cdot \vec{F}(Q_i)) + \frac{1}{|V_i|} \sum_{f \in \partial V_i} \sum_l \alpha_{j,f,l} [F^n]_{f,l} S_f = 0. \quad (2.12)$$

With a judicious choice of solution and flux points, as shown in Figure 1, solution reconstruction can be avoided. Other advantages include an identity mass matrix, and easy extension to mixed elements such as prismatic, and pyramidal cells in 3D. For curved iso-parametric elements, the CPR formulation is applied to the transformed

equation on a standard element. The application of the CPR formulation to hybrid meshes is quite straight forward. It has been successfully applied to arbitrary 2D hybrid meshes.

2. Multi-p residual-based error indicator

To present the basic idea, we assume that the solution is sufficiently smooth, and p-refinement is chosen. Let the (nonlinear) differential operator be L , and the differential equation be denoted by $L(Q) = 0$ with Q the exact solution. Denote L^{Hp} the discrete CPR operator on a mesh of size H with a given polynomial degree p , and Q^{Hp} the numerical solution. Obviously, we have

$$L^{Hp}(Q^{Hp}) = 0. \quad (2.13)$$

Let's assume the numerical solution is reasonably close to the exact solution. The solution error should then be $(p+1)$ th order.

Then, we could interpolate or prolongate the lower order (degree p) solution to a higher order P (e.g. $P = p+1$) solution space. The residual of the higher order operator on the prolonged solution can serve as an error estimate. Let the prolonged solution be Q^{HP} . Denote this interpolation operator I_p^P , then

$$Q^{HP} = I_p^P Q^{Hp} \quad (2.14)$$

The defect is defined as $d^{HP} = I_p^P [L^{Hp}(Q^{Hp})] - L^{HP}(I_p^P Q^{Hp})$, where L^{HP} is the discrete higher order operator. Ideally, the first term $I_p^P [L^{Hp}(Q^{Hp})]$ should be 0, but in real applications, the solution does not need to converge completely in order to calculate d^{HP} . Experiences with multigrid-based error estimators indicate the defect d^{HP} is an excellent indicator of the error sources, which generate solution errors to appear possibly at other regions because of the transport nature of the governing equations.

Then, the defect is localized to each cell by

$$\eta_i = \frac{1}{V_i} \int_{V_i} |d_i^{HP}| dV. \quad (2.15)$$

The quantity η_i is then used as the error indicator to drive the hp-adaptation. Note that the more expensive high-order residual operator is only used once during the evaluation of η_i , without the need to solve any non-linear high-order problem. Therefore, this operation requires even less computing power than an explicit time marching.

Once the cellwise residual error indicator η is computed for each cell in the domain by Eqn. (2.15), a fixed fraction approach is employed to determine the cells adaptations will be applied to. This approach flags a fixed portion (e.g. $f_{adapt} = 0.1$) of the total cells with the largest error indicator η . Whether h- or p-adaptation is applied will be decided by the AP-TVD marker.

3. Accuracy-preserving TVD marker

The AP-TVD limiter is used as a smoothness indicator to flag the non-smooth regions of the flow field, such as flow discontinuities. In the flagged regions, h-adaptation is the preferred approach. Once a cell is flagged by the AP-TVD marker, a

The procedure of the AP-TVD marker is divided into two steps:

1. Compute the cell averaged solutions at each cell. Then compute the min and max cell averages for cell I from a local stencil including all of its node neighbors, i.e.,

$$\bar{Q}_{i,\min} = \min\left(\bar{Q}_i, \min_{1 \leq r \leq nb} \bar{Q}_r\right), \bar{Q}_{i,\max} = \max\left(\bar{Q}_i, \max_{1 \leq r \leq nb} \bar{Q}_r\right) \quad (2.16)$$

2. Cell i is considered a candidate for trouble cell if, for any solution point j ,

$$Q_{i,j} > 1.01\bar{Q}_{i,\max} \quad \text{or}$$

$$Q_{i,j} < 0.99\bar{Q}_{i,\min} \quad (2.17)$$

The constants 1.01 and 0.99 are not problem dependent. They are simply used to overcome machine error, when comparing two real numbers, and to avoid the trivial case of when the solution is constant in the region.

3. This step aims to unmark those cells at local extrema that are unnecessarily marked in the last step. Here, for a given marked cell, a minmod TVD function is applied to verify whether the cell-averaged 2nd derivative is bounded by the slopes computed by cell-averaged 1st derivatives.

Assume cell i is a marked cell in step 2, cell nb is a face neighbor of cell i , the unit vector in the direction connecting the cell centroids of cell i and nb is $\vec{l} = (l_x, l_y)$. The cell averaged 2nd derivative in this direction is

$$\bar{Q}_{i,ll} = \bar{Q}_{i,xx}l_x^2 + 2\bar{Q}_{i,xy}l_xl_y + \bar{Q}_{i,yy}l_y^2 \quad (2.18)$$

In a similar manner, the cell-averaged first derivative in l direction, for both i -th and nb -th cells, can be computed as

$$\bar{Q}_{i,l} = \bar{Q}_{i,x}l_x + \bar{Q}_{i,y}l_y \quad \bar{Q}_{nb,l} = \bar{Q}_{nb,x}l_x + \bar{Q}_{nb,y}l_y \quad (2.19)$$

Then, the estimation of the 2nd derivative can be obtained as

$$\tilde{Q}_{i,ll} = \frac{\bar{Q}_{nb,l} - \bar{Q}_{i,l}}{|\vec{r}_i - \vec{r}_{nb}|} \quad (2.20)$$

Then define a scalar limiter for this face as

$$\phi_{i,nb}^{(2)} = \min \text{mod} \left(1, \frac{\beta \tilde{Q}_{i,ll}}{Q_{i,ll}} \right), \quad (2.21)$$

where $\beta=1.5$. This process is repeated for every face neighbor, and minimum of all computed $\phi_{i,nb}^{(2)}$ is obtained

$$\phi_i^{(2)} = \min_{nb} \phi_{i,nb}^{(2)} \quad (2.22)$$

if $\phi_i^{(2)} = 1$, then cell i is unmarked as a non-smooth cell. If $\phi_i^{(2)} < 1$, the cell is confirmed as a trouble cell, and flagged for h-adaptation.

The above non-smoothness marker can be applied only when polynomial degree $p > 1$ (3rd order and up) for cell i . For those cell with $p=1$, a similar procedure involving the cell-averaged 1st derivatives is used. However, the marker for $p=1$ is unable to unmark the smooth extremas as the above limiter. Therefore, for cases that have both h- and p-adaptation, the base solution is always computed with 3rd order scheme.

III. Mesh Adaptation

1. Non-conformal interfaces in hp-adaptation

Changing the h- and p-levels for cells will inevitably create non-conformal interfaces between cells. When a cell is h-adapted, the cell is divided into four new ones by connecting the center of each face, for both triangular and quadrilateral cases. A hanging node is resulted in the adapted mesh between different h-levels. For p-adaptation, the interface between cells with different p-level is also non-conformal, since the flux points on opposing sides support polynomials of different degrees. Special treatment is required when computing the common numerical flux on these non-conformal interfaces.

In the current study, a set of rules are observed when flagging the cells for adaptation. They help achieve a smooth adaptation, also limit the type of interfaces to be dealt with. The rules are listed as follows:

1. The difference of p-levels between neighboring cells are no larger than 1.
2. The difference of h-levels between neighboring cells are no larger than 1, i.e. only one level of hanging nodes are allowed.
3. If one interface has different p-levels on both sides, the h-levels have to be the same.
4. If one interface has different h-levels on both sides, the p-levels have to be the same.

Each time the mesh is adapted, necessary adjustments are made to ensure that the rules above are observed over the whole domain.

When the rules above are enforced, there leaves only three types of interfaces: the normal conformal interfaces, the p-interfaces with the same h-level, and the h-interfaces with the same p-level.

For a non-conformal interface, an intermediate ‘‘mortar face’’ [13] (Figure 2b) is constructed to link the two faces in different solution space. The mortar faces always take the space of the higher p- or h-level of the two sides. First, the solutions from the lower p- or h-level are interpolated or prolonged to the mortar face level. Then, the calculation of common numerical fluxes F_{com}^n takes place on the mortar face. Last, the resulted common fluxes need to be projected back to the lower p- or h-space.

The interpolation process is quite straightforward. For both types of interfaces we are dealing with, the lower p- or h-space is always included in the higher p- or h-space, so the same polynomial are used to obtain more point values that match the flux points on the other side. For the restriction on the last step, we use the following

$$\int_f W_j F_n^{h,p} dS = \int_f W_j F_n^{h,p} dS, \quad (3.1a)$$

$$\int_f W_j F_n^{h,p} dS = \int_f W_j F_n^{H,p} dS, \quad (3.1b)$$

where W_j ($j=1\dots p+1$) are the basis of p -th degree polynomial. Note that when $W=1$, the conservation condition is automatically satisfied. Eqn (3.1a) is used for p-interface while (3.1b) for h-interface.

One example of this procedure is shown in Figure 2, which is a p-interface with $p-1$ on one side and $p-2$ on the other (Figure 2a). The $p=1$ solution is interpolated to $p=2$ (Figure 2b), and the Riemann flux is computed on the mortar face. After that, the resulting F_{com}^n is projected to p-1 space using (3.1a) for use in the p-1 cell (Figure 2c). A similar procedure is followed for h-interfaces.

2. The adaptation procedure

The procedure for p-adaptation for steady flow is listed as follows:

1. Solve the flow field until a convergence criterion is reached.
2. Follow the procedure in Section 2.2, compute η_i for each cell.
3. Flag a fixed fraction of all the cells with largest error indicator.
4. Make necessary adjustments to enforce the rules in Section 3.1.
5. Update the mesh, metric terms and connectivities. Inject the solution to new p-levels.
6. Repeat step 1-5.

For hp-adaptation, the starting solution is always computed with uniform $p=2$, in order to use the AP-TVD limiter to correctly identify the non-smooth regions. Once the non-smooth region is flagged, the order of accuracy is dropped to $p=1$. The procedure of hp-adaptation is described as follows.

1. Start the computation with uniform $p=2$ over the whole domain.
2. Solve the flow field until residual stops changing.
3. Flag all the cells that have been marked in the last five iterations for h-adaption.
4. Follow the procedure in Section 2.2, compute η_i for each cell, select a fixed fraction of cells with the largest η_i .
5. Search the neighbors of the cells flagged in step 3, if a neighboring cell has a large η_i , it is also flagged for h-adaptation. Also flag all the h-adapted cells for p-coarsening, reduce their order of accuracy to $p=1$.
6. Apply p-adaptation to smooth regions.
7. Update the mesh, metric terms and connectivities. Inject the solution to new h/p-levels.

8. Repeat steps 2-7.

The adaptation can keep going until desired number of levels is reached, or an output of interest stops changing.

IV. Numerical Tests

1. P-adaptation for a subsonic flow over a Gaussian bump

The flow over a Gaussian bump is computed with the computational domain shown in Figure 3. The incoming flow has a Mach number of 0.5. Wall boundary is applied for the bump (bottom boundary), characteristic boundary for both inlet and outlet, and symmetry for the top boundary.

The solver starts from uniform 2nd order scheme, and then undergoes six loops of p-adaptation. Adaptation fractions $f_{\text{adapt}} = 0.1$ and $f_{\text{adapt}} = 0.2$ are used.

Figure 4 shows the final adaptation results of the $f_{\text{adapt}} = 0.2$ case. It can be seen the residual-based indicator clearly identify the error source (the bump in this case). The closer to the bump, the adaptation has been applied.

Figure 5 shows the Mach contour of the final solution of the $f_{\text{adapt}} = 0.2$ case. Although the cells have been adapted into 6 different p-levels, the solution is kept rather smooth by the mortar face configuration at p-interfaces.

L_2 entropy error over the whole domain is used as a measure of accuracy, defined by

$$\|\Delta_{\text{ent}}\|_{L_2} = \sqrt{\frac{\int_{\Omega} \left(\frac{p / \rho^\gamma - p_\infty / \rho_\infty^\gamma}{p_\infty / \rho_\infty^\gamma} \right)^2 dV}{\int_{\Omega} dV}}. \quad (4.1)$$

The entropy error of the p-adaptation cases are compared with uniform p-refinement in Figure 6. Entropy error is effectively reduced by the p-adaptation. The same level of error is achieved with much fewer DOFs than the uniform p-refinement.

2. P-adaptation for a subsonic flow over the NACA0012 airfoil

Next, the p-adaptation is tested in the subsonic flow over the NACA 0012 airfoil, with $Ma=0.3$ and $AOA=5\text{deg}$. The hybrid mesh used for this case (as shown in Figure 7a) is constructed with an arbitrary mix of quadrilateral and triangular cells. The adaptation starts from a very crude 2nd order solution (Figure 7b), undergoes five levels of p-adaptation, also with $f_{\text{adapt}} = 0.1$ and $f_{\text{adapt}} = 0.2$.

Figure 8 shows the result of the p-adaptation. The region near the airfoil surface is repeatedly adapted to a very high p-level. The region near the leading edge is also identified as a main source of the residual error. The Mach contour of the final solution is shown in Figure 9.

Figures 10a-b shows the L_2 entropy error and the error of the drag coefficient respectively. For both errors, the p-adaptation scheme demonstrates more efficient error reduction with less DOFs. Note that the entropy error stops converging after the solution reach a certain p-level, due to the large entropy production near the trailing edge.

3. Hp-adaptation for a transonic flow over the NACA0012 airfoil

The computation of a transonic flow over the same airfoil is used to test the hp-adaptation scheme. For this flow, $Ma=0.8$ and $AOA=1.25\text{ deg}$. Shockwaves are expected on both upper and lower surface of the airfoil, where h-adaptation should be applied, while p-adaptation is applied to smooth parts of the flow field.

The base mesh is shown in Figure 11. First, a 3rd order base solution is computed, and the AP-TVD limiter is used to identify the shockwaves and other unsmooth regions. Once flagged as non-smooth, the region is reduced to 2nd order accuracy and no p-adaptation is allowed.

Figure 12 shows the hp-adaptation results after 3 levels of adaptation. We can see that the shockwave regions are correctly detected and repetitive h-adaptation is applied in this region. The region near the trailing edge is also h-adapted. P-adaptation is applied to the non-flagged regions, as cells with higher p-levels are found near the leading edge.

The density contours of the final solution are shown in Figure 13. With much finer mesh due to the h-adaptation, the shockwave is well resolved, while smooth solution is obtained in the p-adapted regions, with minor oscillation behind the shockwave.

V. Conclusion

A residual-based error indicator is developed to drive an hp-adaptation procedure in the current study. The AP-TVD troubled cell marker serves as the smoothness indicator to decide whether h- or p- adaptation should be applied to a certain region. The residual-based indicator requires much less computing cost compared with the more sophisticated adjoint-based error indicators. It is also more rigorous than the gradient or feature based approaches.

Several typical numerical tests of inviscid flow have been conducted. For smooth flow fields, the p-adaptation driven by the residual-based indicator effectively targets the error source. The adaptation procedure is shown to improve the numerical solution visually, as well as achieve the same error level with fewer DOFs. Hp-adaptation is also tested on a transonic flow with shockwaves. The non-smooth regions of the flow field is correctly detected by the AP-TVD marker, where h-adaptation is applied, while p-adaptation is applied to the smooth regions. High-quality solution can be achieved with relatively low cost after the adaptation. These test cases show the potential of the residual-based adaptation procedure in complex CFD problems.

Acknowledgments

The present study was funded by AFOSR grant FA9550-06-1-0146. The views and conclusions contained herein are those of the authors and should not be interpreted as necessarily representing the official policies or endorsements, either expressed or implied, of AFOSR or the U.S. Government.

References

- [1] M. Ainsworth, J.T. Oden, A unified approach to a posteriori error estimation using element residual methods, *Numer. Math.* 65 (1993) 23–50.
- [2] T.J. Baker, Mesh adaptation strategies for problems in fluid dynamics. *Finite Elem Anal Des* 1997;25:243–73.
- [3] F. Bassi and S. Rebay, High-order accurate discontinuous finite element solution of the 2D Euler equations, *J. Comput. Phys.* 138, 251-285 (1997)
- [4] C.E. Baumann, T.J. Oden, A discontinuous hp finite element method for the Euler and Navier–Stokes equations. *Int J Num Meth Fluids* 1999;31(1):79–95.
- [5] M. J. Berger and P. Collela, Local adaptive mesh refinement for shock hydrodynamics, *J. Comput. Phys.*, vol. 82, pp. 64-84, 1989.
- [6] R. Biswas, K.D. Devine, and J. Flaherty, Parallel, adaptive finite element methods for conservation laws, *Appl. Numer. Math.*, 14, 1994, pp. 255–283.
- [7] B. Cockburn and C.-W. Shu, The Runge-Kutta discontinuous Galerkin method for conservation laws V: multidimensional systems, *J. Comput. Phys.*, 141, 199 - 224, (1998).
- [8] M. B. Giles and N. A. Pierce. Adjoint equations in CFD: Duality, boundary conditions and solution behavior. *AIAA paper* 97-1850, 1997.
- [9] R. Harris and Z.J. Wang, “High-order adaptive quadrature-free spectral volume method on unstructured grids,” *Computers & Fluids* 38 (2009) 2006–2025.
- [10] R. Hartmann and P. Houston. Adaptive discontinuous Galerkin finite element methods for the compressible Euler equations. *J. Comput. Phys.*, 183:508–532, 2002.
- [11] H.T. Huynh, A flux reconstruction approach to high-order schemes including discontinuous Galerkin methods, *AIAA Paper* 2007-4079.
- [12] H. Jasak, A.D. Gosman, Residual error estimate for the finite-volume method, *Numerical Heat Transfer*, 39:1-9, 2001.
- [13] Y. Li, S. Premansuthan and A. Jameson, Comparison of h- and p-adaptations for spectral difference method, *AIAA* 2010-4435.
- [14] Y. Liu, M. Vinokur and Z.J. Wang, Three-Dimensional High-Order Spectral Finite Volume Method for Unstructured Grids, *AIAA-2003-3837*.
- [15] Y. Liu, M. Vinokur, and Z.J. Wang, Discontinuous Spectral Difference Method For Conservation Laws On Unstructured Grids, *Journal Of Computational Physics* Vol. 216, pp. 780-801 (2006).
- [16] M. A. Park. Adjoint-based, three-dimensional error prediction and grid adaptation. *AIAA paper* 2002-3286, 2002.
- [17] Shih, T.I-P. and Qin, Y., A Posteriori Method for Estimating and Correcting Grid-Induced Errors in CFD Solutions – Part 1: Theory and Method, *AIAA Paper* 2007-100.
- [18] L. Wang and D. Mavriplis, Adjoint-based h-p Adaptive Discontinuous Galerkin Methods for the Compressible Euler Equations, *AIAA-2009-0952*.

- [19] D.A. Venditti, D.L. Darmofal, Adjoint error estimation and grid adaptation for functional outputs: Application to quasi-one-dimensional flow. *J Comput. Phys.* 2000;164:204–27.
- [20] D.A. Venditti, D.L. Darmofal, Anisotropic grid adaptation for functional outputs: application to two-dimensional viscous flows, *J. of Comp. Phys.*, 187 (2003) 22-46.
- [21] Z.J. Wang, Spectral (Finite) volume method for conservation laws on unstructured grids: basic formulation, *J. Comput. Phys.* Vol. 178, pp. 210-251, 2002.
- [22] Z.J. Wang and H. Gao, A Unifying Lifting Collocation Penalty Formulation for the Euler Equations on Mixed Grids, AIAA-2009-401.
- [23] M. Yang and Z.J. Wang, A parameter-free generalized moment limiter for high-order methods on unstructured grids, AIAA-2009-605.
- [24] X.D. Zhang, J.-Y. Trepanier, R. Camarero, A posteriori error estimation for finite-volume solutions of hyperbolic conservation laws, *Comput. Methods Appl. Mech. Engrg.* 185 (2000).

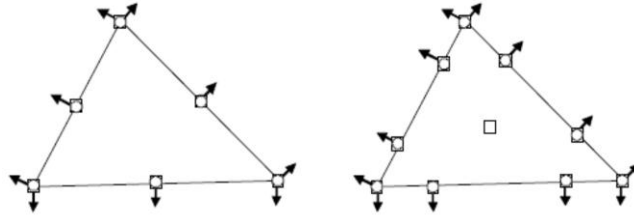


Figure 1. The configuration of solution points (square) and flux points (circle) of p-2 and p-3 CPR method.

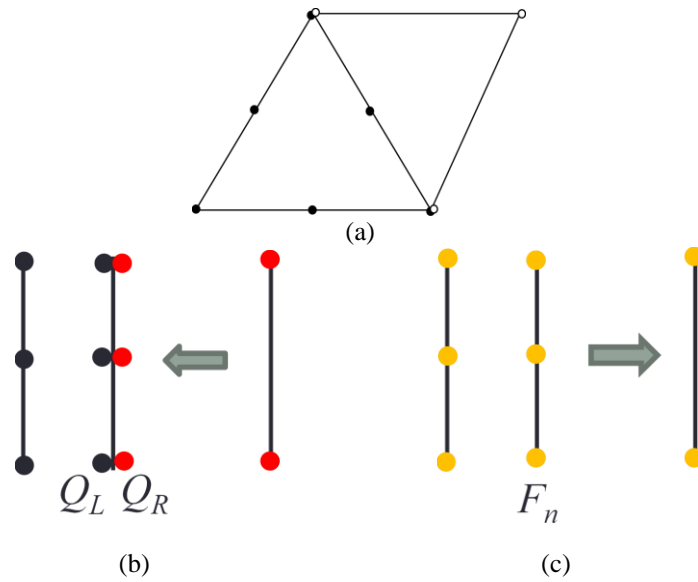


Figure 2. Demonstration of a mortar face procedure for a p-interface. (a) P-interface. (b) Prolongation of the lower order solution (c) Restriction of the common numerical flux.

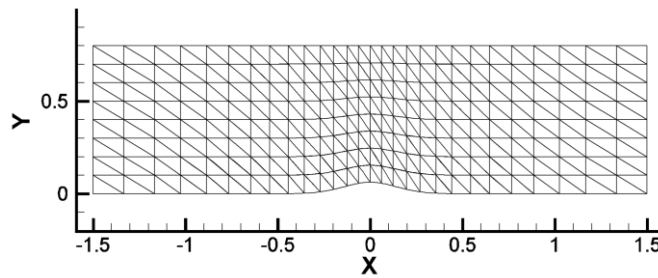


Figure 3. The computational domain and mesh for the subsonic bump flow

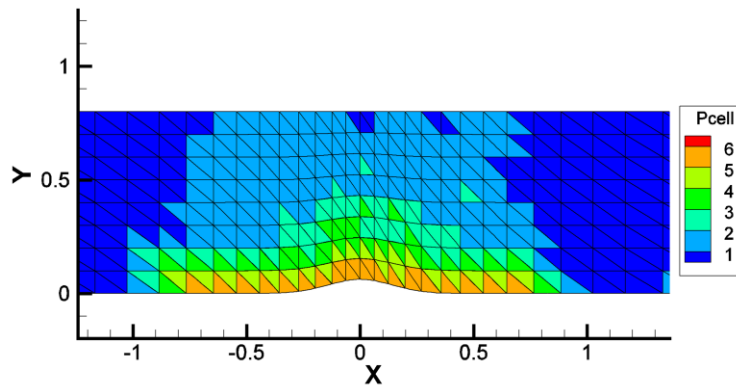


Figure 4. The result of p-adaptation for subsonic bump flow, $f_{\text{adapt}} = 0.2$.

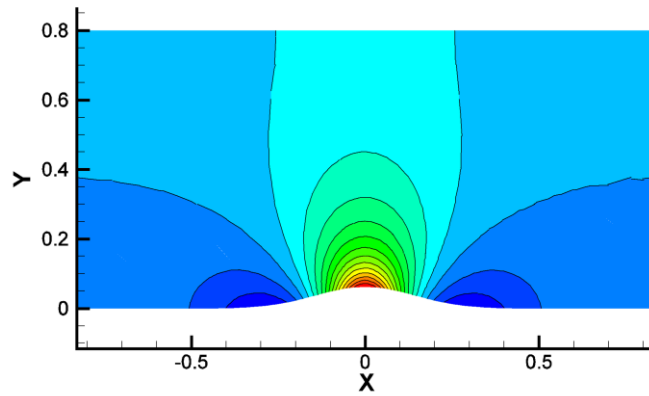


Figure 5. The Ma contours for the bump flow after p-adaptation.

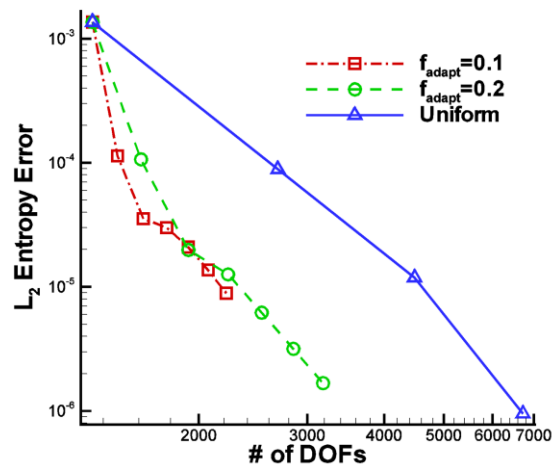


Figure 6. The L_2 entropy error from p-adaptation and uniform p-refinement.

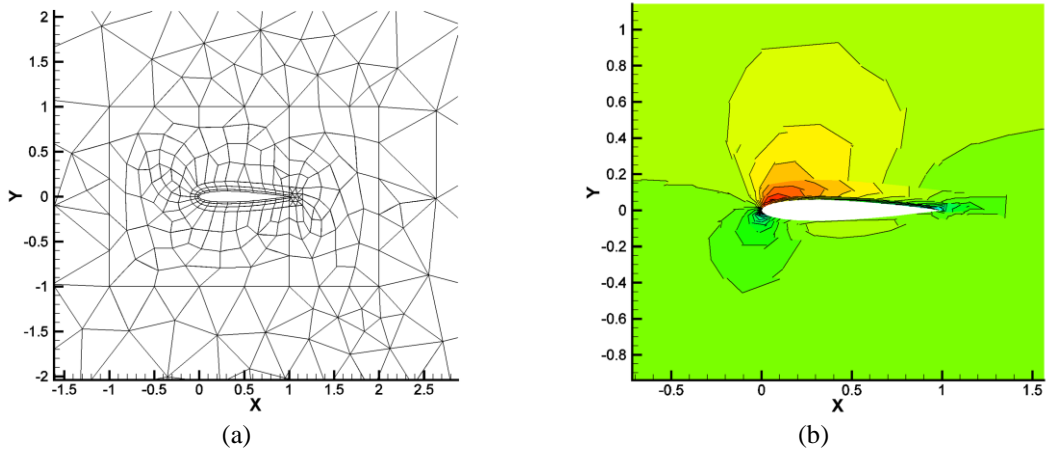


Figure 7. (a) Hybrid mesh for subsonic flow over NACA 0012 airfoil. (b) Ma contour of the initial 2nd order solution.

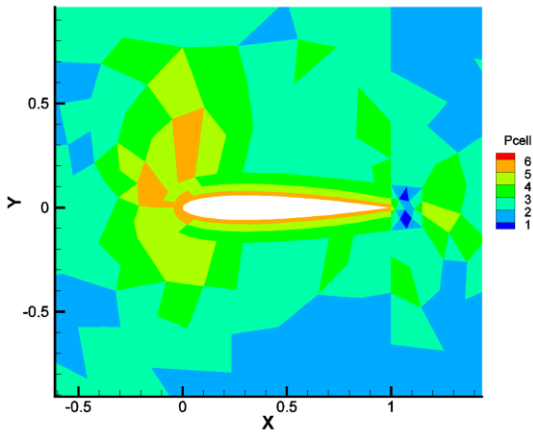


Figure 8. P-adaptation results for the subsonic flow over NACA0012 airfoil.

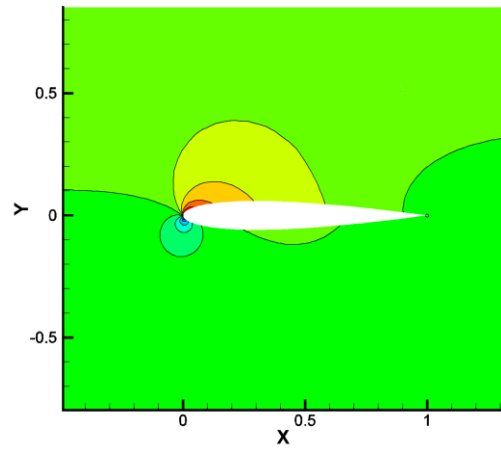


Figure 9. Ma contour of subsonic airfoil flow after p-adaptation.

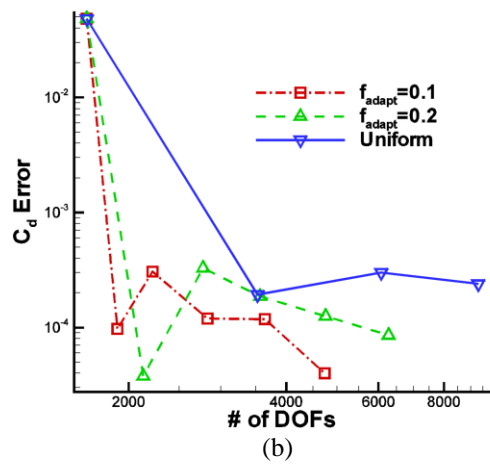
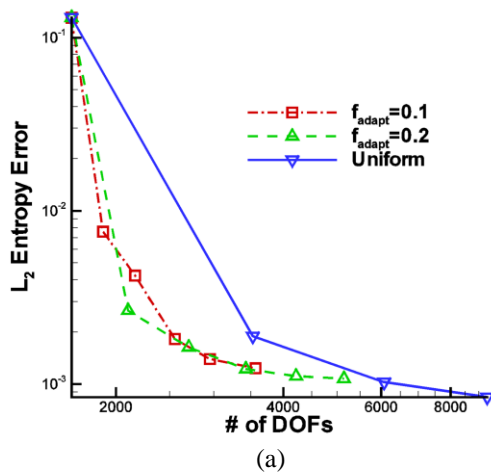


Figure 10 (a) L_2 entropy error (b) drag coefficient error for the subsonic airfoil flow.

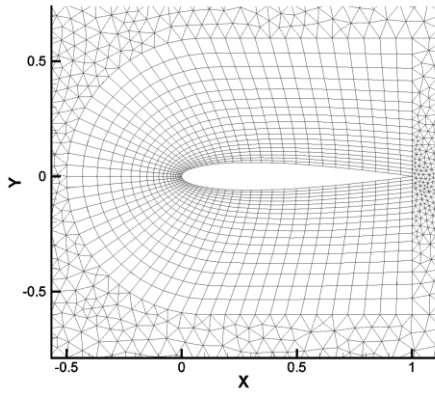


Figure 11. Initial mesh for the transonic airfoil flow.

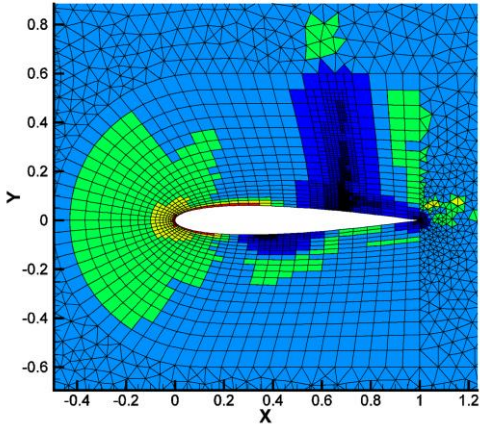


Figure 12. hp-adaptation results for the transonic airfoil flow.

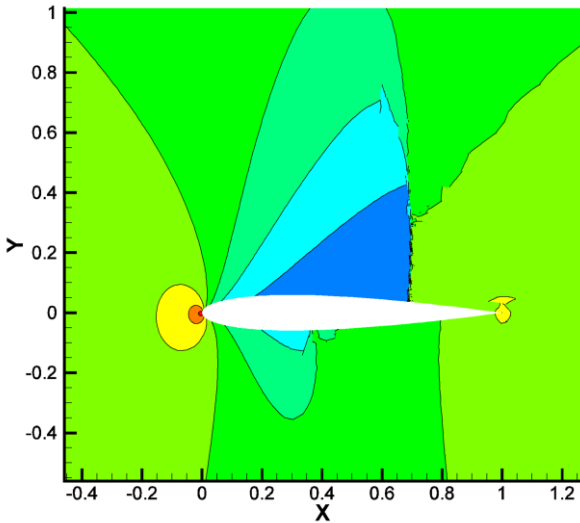


Figure 13. Density contours for the transonic airfoil flow after hp-adaptation.